Journal of Materials Chemistry C

ROYAL SOCIETY OF CHEMISTRY

PAPER

View Article Online
View Journal | View Issue

Cite this: J. Mater. Chem. C, 2022, 10, 5514

Anomalies in the bulk and surface electronic properties of SnS: effects of native defects†

Rohit Dahule, [a] Chetan C. Singh,[a] Kenta Hongo,[bc] Ryo Maezono[b] and Emila Panda*[a]

Received 5th October 2021,
Accepted 26th February 2022

DOI: 10.1039/d1tc04738h

rsc.li/materials-c

SnS is a promising photovoltaic absorber material because of its low cost and lower toxicity and is usually present in a heterostructure. Understanding the bulk and the surface electrical properties would help in the understanding of the transport behavior and hence would be extremely useful in fabricating high performance devices. In this regard, here a combinatorial approach of experiment and theory was used to understand the anomalies in the bulk and the surface electrical properties of SnS. Experimentally, single phase polycrystalline SnS films are fabricated by RF magnetron sputtering and characterized for their detailed microstructure, and optical, bulk and surface electrical properties. The observed anomalies in their bulk and surface electrical properties are then interpreted through first-principles density functional theory (DFT) calculations of the bulk and the surface electronic structures. DFT calculations on various native surface defects provided further insights into the experimentally observed semi-metallic behavior using scanning tunnelling spectroscopy.

1. Introduction

Tin mono-sulfide (SnS) is a promising absorber material for the thin-film photovoltaic (PV) technology, as it is a low cost, less toxic, and earth-abundant semiconductor with a direct band gap of 1.3–1.5 eV and has a high absorption coefficient ($>10^4$ cm^{-1}).[1] Intrinsically, it is of p-type with a theoretical efficiency of 32% for a single-junction cell. Despite this, the device efficiency of SnS solar cells remains poor, with the highest reported efficiency being 4.63%.[2] Moreover, the poor performance of SnS-based solar cells is mainly attributed to the uncertainty in their electrical properties, because of the presence of a large number of native point defects in the bulk.[3,4] Besides, the surface electrical properties of this absorber material play an equally important role as this layer is usually present in a stack, thus affecting the electrical properties of the entire heterostructure and thereby the device efficiency.[5–7] This is because surfaces could have completely different electronic structures than their bulk owing to the relaxation of the surface atoms. Additionally, appearance of native point defects on the SnS surface could completely alter the band structure, further altering the transport properties. Furthermore, surface defects can be harmful as these could act as recombination centres for photogenerated electron–hole pairs, thereby degrading the photovoltaic performance.[8] This necessitates the fundamental understanding of these band structures and thereby associated electrical properties for preparing efficient photovoltaic devices.

To this end, here, a combinatorial approach of experiment and theory was used to understand the anomalies in the (defect-induced) surface and bulk electrical properties of SnS. Experimentally, SnS films are fabricated by varying the substrate temperature (T_s) from 303 to 623 K on the soda lime glass (SLG) substrate, for 60 min using radio frequency (RF) magnetron sputtering. RF magnetron sputtering is used here as this is a well-known technique for depositing high-quality thin films and is commercially adopted for fabricating thin film solar cells. Following fabrication, a detailed investigation on the microstructure, and optical, bulk and surface electrical properties of these films is carried out using a combination of experimental techniques. First-principles density functional theory (DFT) calculations are then performed on the SnS orthorhombic crystal structure to compute its electronic structure, as this is (experimentally) observed to be the most preferred crystallographic orientation. Moreover, DFT calculations are applied to the SnS (111) surface structures with the inclusion and exclusion of various native defects of vacancies, interstitials and antisites in order to investigate differences in electronic structures between

[a] Materials Engineering Discipline, Indian Institute of Technology, Gandhinagar, Palaj-382355, Gujarat, India. E-mail: emila@iitgn.ac.in
[b] School of Information Science, Japan Advanced Institute of Science and Technology (JAIST), 1-1 Asahidai, Nomi, Ishikawa 923-1292, Japan
[c] Research Centre for Advanced Computing Infrastructure, JAIST, 1-1 Asahidai, Nomi, Ishikawa 923-1292, Japan

† Electronic supplementary information (ESI) available: Schematics of bulk SnS and SnS (111) surface supercells. Selection of suitable surface defect sites of vacancies, interstitials and antisites. The ionic displacements of the atoms in the top slab for the SnS (111) surface supercell and the SnS (111) surface supercell with various defects. See DOI: 10.1039/d1tc04738h

the defective and defect-free surfaces by comparing with the bulk. In the end, a correlation between the theoretical data and the experimental observations is established.

Though extremely relevant, studies addressing both the theory and experiment are found to be scarce in the literature. Whereas, the experimental approach in the literature mostly focused on the fabrication and bulk optoelectronic properties of SnS thin films, theoretical studies mostly aimed at understanding the electronic structure, the band gap and the thermodynamics of the native defect states in its bulk.[3,4,9] To the best of our knowledge, we have, for the first time, made detailed experimental and theoretical studies addressing both inclusive and exclusive of native defects on the SnS (111) surface.

2. Methods

2.1. Thin film fabrication and characterization

A series of SnS films were deposited on ultrasonically cleaned 1 cm × 1 cm soda lime glass (SLG) substrates (supplier: Ted Pella, Inc.) at substrate temperatures (T_s) of 303 K, 573 K and 623 K for 60 min. A constant RF power of 50 W was provided to the target (target: SnS; supplier: Able Target Corporation; 2'' diameter and 3 mm thick); a chamber pressure of 11.0 × 10^{-3} mbar was maintained during the entire deposition process by providing 40 SCCM argon gas (of 99.99% purity). The optimized substrate rotation and substrate to target distance of 15 rpm and 7.0 cm respectively were used here.

Detailed structural, chemical, optical, and electrical characterization studies of these films were carried out using experimental techniques as elaborated in the following. The phase and the crystallite size of these deposited films were determined using Grazing Incidence X-ray diffractometry (GIXRD; model: D8 Discover, supplier: Bruker Corporation) at a glancing angle of 6° in the 2θ range of 20–80° (step size of 0.02°) using Cu K_α (λ = 0.15418 nm) radiation. The surface topography of these films was characterized using Atomic Force Microscopy (AFM; model: Nanoscope Multimode 8.0, supplier: Bruker Corporation). Surface chemical states were analyzed using X-ray photoelectron spectroscopy (XPS; model: PHI 5000 Versa Prob II, supplier: ULVAC-PHI, Inc.). The elemental chemical compositions of these deposited films were investigated using energy dispersive X-ray spectroscopy along with FESEM (EDS, model: AZtec, supplier: Oxford Instrument). The optical properties (*i.e.*, transmittance and the optical band gap) of these SnS films were investigated using a UV-vis-NIR spectrophotometer (model: Cary 5000, supplier: Agilent Technologies) in the wavelength range of 300–2500 nm. A Hall effect measurement system (HEMS; model: 8404 AC/DC HMS, Lakeshore) in the van der Pauw configuration was used for measuring the bulk electrical resistivity, carrier concentration and carrier mobility of these films.

Additionally, the local (nanoscale) surface electrical properties of these SnS films were measured using scanning tunnelling microscopy/spectroscopy (STM/STS; the module of a scanning probe microscope (SPM)) under ambient conditions. STM images were acquired using a Pt/Ir tip (PT-10; supplier: Bruker Corporation) of 0.25 mm diameter and 8 mm length, following which local STS *I–V* characteristics were recorded at 21 different locations from each of these captured 1 μm × 1 μm STM images by applying a bias voltage of ±0.8 V. To maintain the electrical continuity while performing STM/STS measurement, silver paint was used for grounding the bottom metal plate and the top SnS thin film.

2.2. Computational methodology

To address the experimentally observed anomalies between the surface and the bulk optoelectronic properties, density functional theory (DFT)[10,11] calculations were used to compute the electronic structures of the pristine/defect-free and defective SnS surfaces as well as the bulk, which involves constructing their structural models; see Fig. S1 and S2 in the ESI† for details. An orthorhombic crystal structure with 8 atoms (*i.e.*, Sn_4S_4) in its supercell was used for the bulk SnS structure. Since our experiment indicated (111) as the most oriented SnS film, this surface was considered and modelled by the supercell method: slabs with the (111) surface orientation. To avoid the interaction between these surfaces in the perpendicular direction, these slabs were separated by inserting a vacuum layer. Constructing the SnS (111) surface slab with 16 atoms (*i.e.*, Sn_8S_8; 5.909 Å thickness), the SnS (111) surface supercell was constructed from three of the slabs with an intermediate vacuum thickness of 15 Å, where the top surface was composed of 4 Sn and 4 S atoms as shown in Fig. 1. Note that the atoms in the bottom slabs have been keptfixed during structural optimization to mimic the bulk-like characteristic. Based on the defect-free surface, the defective surfaces were constructed by introducing a range of neutral defects of tin and sulfur: vacancies (V_{Sn} and V_S) and interstitials (Sn_i and S_i) were formed by removing and adding one atom from and to the top surface of the SnS (111) surface supercell, respectively. Similarly, antisites (Sn_S and S_{Sn}) were created by substituting one type of atom with the other. Our structural models were visualized using the Visualization for Electronic and Structural Analysis (VESTA) software.[12]

Our DFT simulations were performed using the Vienna *Ab initio* Simulation Package (VASP)[13,14] and were used to first compute the bulk and the surface electronic structures of defect-free SnS; the Perdew–Burke–Ernzerhof (PBE)[15] functional assuming the generalized gradient approximation was adopted as our exchange–correlation functional; the core–valence electron interaction was treated here using the projector augmented wave (PAW)[16] method, where 4d, 5s, and 5p electrons of Sn and 3s and 3p electrons of S were treated as valence electron configurations. In addition, defective surface electronic structures were computed in a similar way to the pristine case,

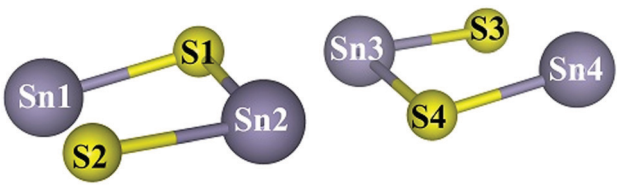

Fig. 1 Top surface of the SnS (111) surface supercell.

thereby investigating the influence of various thermodynamically stable native defect states on the surface electronic structure of SnS. Computational details of DFT settings are as follows: converged $3 \times 7 \times 7$, $7 \times 9 \times 9$ and $7 \times 9 \times 1$ Monkhorst–Pack K-point grids[17] were used for the computations of the bulk, (111) bulk, and (111) surface of SnS, respectively; a cut off energy of 450 eV was used for the plane wave expansion. In the case of surfaces, a dipole correction along the z-axis was employed to remove the artificial electric field in the vacuum region.[18] The geometry optimizations were performed with thresholds for the energy (1.0×10^{-8} eV per cell) and force (0.01 eV Å^{-1}) convergences.

In order to compare and understand the relative stabilities of various surface defects, their formation energy ($E^f[X]$) was calculated by using the following relation:[19]

$$E^f[X] = E_{total}[X] - E_{total}[0] - \sum_i n_i \mu_i, \quad (1)$$

where $E^f[X]$ is the formation energy of a defect X, $E_{total}[X]$ is the total energy derived from a supercell calculation containing the defect X, $E_{total}[0]$ is the total energy of the perfect crystal using an equivalent supercell (without the defect), n_i is the number of atoms of type i (host or impurity atoms) that have been added to ($n_i > 0$) or removed from ($n_i < 0$) the supercell to form the defect, and μ_i is the corresponding chemical potential of these species.

To calculate the chemical potentials of Sn and S under Sn- and/or S-rich conditions, the following boundary criteria were considered:

$$\mu_{Sn} + \mu_S \leq \mu_{SnS,bulk}, \quad (2)$$

$$\mu_{Sn} \leq \mu_{SnS,bulk}, \quad (3)$$

$$\mu_S \leq \mu_{SnS,bulk}, \quad (4)$$

where μ_{Sn} and μ_S are the chemical potentials of defect forming species of Sn and S, respectively; $\mu_{SnS,bulk}$, $\mu_{Sn,bulk}$ and $\mu_{S,bulk}$ represent the chemical potentials of bulk SnS, Sn, and S atoms, respectively. Note that the total energies of each of these structures per formula unit were computed and then used as chemical potential values. Moreover, μ_{Sn} and μ_S should always be lower than their natural phases of $\mu_{Sn,bulk}$ and $\mu_{S,bulk}$, respectively, otherwise which these natural phases of Sn and S would form instead of SnS.

The formation energy of these native defects at each possible defect sites was calculated to obtain the thermodynamically preferred site. For example, to obtain the preferred V_{Sn} surface site, various possible surface configurations were used by creating Sn vacancies at each possible location of the top SnS (111) surface (*i.e.*, Sn1, Sn2, Sn3 and Sn4; see Fig. 1). Once the thermodynamically preferred defect site for a particular native defect is ascertained, further calculations concerning to the surface electronic structures such as the band structure and density of states were carried out only for the preferred defect sites. This procedure was followed for all the native defects considered in this study; the details can be found in Section S2 of the SI (ESI†). N.B. in order to avoid the defect-defect interaction, a bigger SnS (111) surface supercell with 32 atoms per slab (*i.e.*, $Sn_{16}S_{16}$) was constructed for calculating the surface electronic structure and the density of states.[20] These preferred sites were found out using the formation energy calculation as for the single native defect.

3. Results and discussion

3.1. Experimental results

Irrespective of T_s, all these deposited films were found to have grown only in SnS chemical composition with a strong (111) orientation (Fig. 2(a)). This is in good agreement with the standard profile of orthorhombic SnS (JCPDS 39-0354) with lattice parameters of a = 11.1923 Å, b = 3.9838 Å, and c = 4.3291 Å. No evidence of secondary phases, such as SnS_2 and Sn_2S_3, was observed. The intensity of the (111) peak was found to be maximum for the SnS film deposited at T_s of 573 K, indicating increased crystallinity at higher T_s. However, at T_s beyond 573 K,

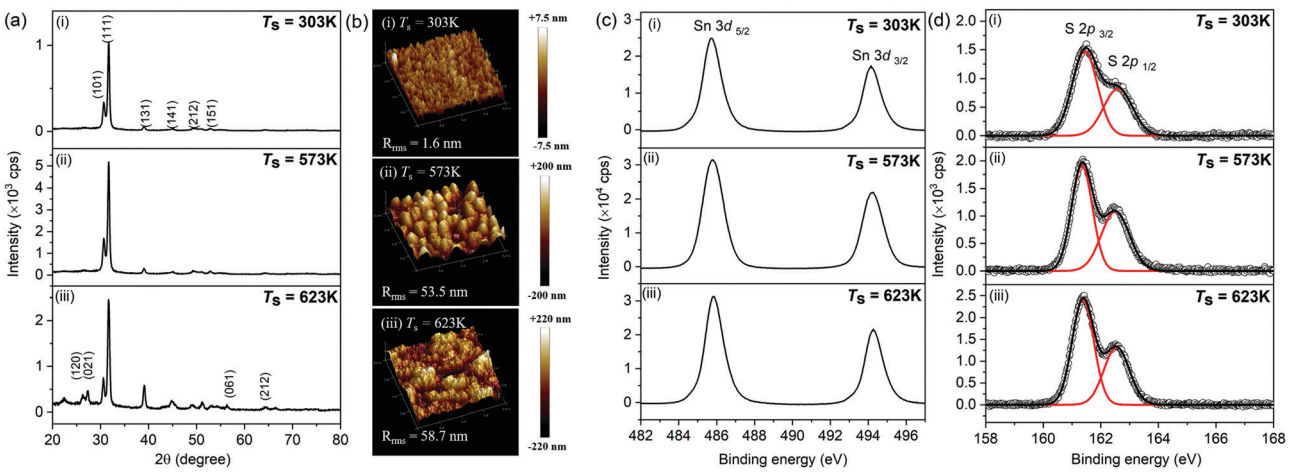

Fig. 2 (a) XRD patterns, (b) AFM micrographs (2 μm × 2 μm), (c) Sn 3d XPS spectra, and (d) S 2p XPS spectra of SnS thin films deposited on soda lime glass substrates at (i) T_s = 303 K, (ii) T_s = 573 K and (iii) T_s = 623 K.

the intensity of the (111) peak reduced, suggesting reduced crystallinity for this film. The average crystallite sizes (D) of SnS films deposited at T_s of 303 K, 573 K, and 623 K corresponded to 22, 32, and 31 nm, respectively.[21] This could be attributed to an increase in the temperature-induced surface diffusion of the incoming sputtering species on the substrate surface with increasing T_s, leading to the faster coalescence of these particles, which would have led to an eventual growth of bigger crystallites.[22,23] The (rms) roughness of these films was found to increase with increasing T_s because of the formation of bigger crystallites at higher T_s (see Fig. 2(b)).

The surface chemical states of SnS films were investigated using XPS to understand the effect of T_s. Fig. 2(c) and 2(d) represent Sn 3d and S 2p core-level XPS spectra, respectively. The binding energy positions of Sn $3d_{5/2}$ and Sn $3d_{3/2}$ were found to be at 485.79 ± 0.02 eV and 494.27 ± 0.01 eV, respectively, with a doublet separation of 8.4 ± 0.01 eV, suggesting Sn in the +2 state.[24] The peaks located at 161.45 ± 0.01 eV and 162.58 ± 0.02 eV with a separation of 1.1 eV are attributed to S $2p_{3/2}$ and S $2p_{1/2}$, confirming the presence of S in the −2 form only.[25] All the SnS films were found to be Sn-rich, with the concentration of Sn (and hence Sn-to-S-ratio) increasing with increasing T_s (see Table 1 shown and discussed later). Note that the Sn-to-S-ratio was found to increase from 1.08 to 1.23 (as measured with XPS) and 1.19 to 1.26 (as measured with EDS) with increasing T_s.

Fig. 3(a) plots the optical transmittance of all the deposited SnS films (in the wavelength range of 300–2500 nm) as a function of T_s. All the films displayed sharp fundamental absorption edges with absorption edge shifting towards a longer wavelength with increasing T_s. Moreover, interference fringes caused by interference between these films and the respective SLG substrates were seen in all the samples, indicating a nearly uniform film with a smooth surface.[26] Their indirect optical band gaps were determined from the intercept of the linear portion of $(\alpha h\nu)^{\frac{1}{2}}$ *vs.* $(h\nu)$ on the *x*-axis using the Tauc equation:

$$(\alpha h\nu) = C(h\nu - E_g)^n, \quad (5)$$

where α is the absorption coefficient, h is Planck's constant, ν is the frequency of radiation, C is a constant, E_g is the optical band gap of the material, and $n = 2$ is for the indirect transition.[27] The indirect band gaps of SnS films deposited at T_s of 303 K, 573 K, and 603 K were found to be 1.62, 1.31, and 1.32 eV, respectively. The variation in the optical bandgap with T_s could be associated with their crystallite size and can be understood by the classical quantum confinement effect.[15,28–30]

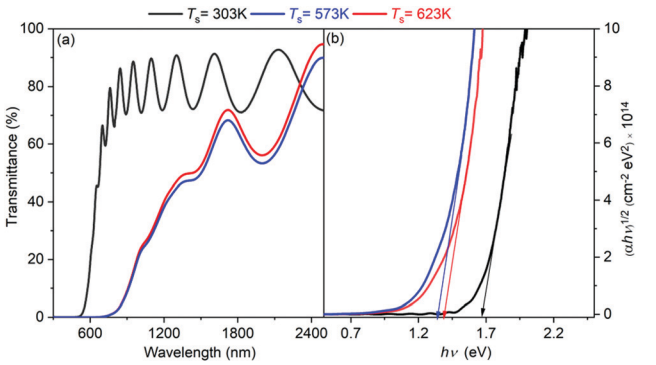

Fig. 3 (a) Optical transmission spectra in the range of 400–2500 nm. (b) Optical band gap of SnS thin films deposited on soda-lime glass substrates at T_s of 303 K, 573 K and 623 K, respectively.

Table 1 shows the variation in the electrical properties (*i.e.*, electrical resistivity (ρ), carrier concentration (p_h), and carrier mobility (μ_h)) of these SnS films with respect to T_s. All these films were found to be of p-type, with holes being the majority charge carriers. p_h was found to decrease from 6.13 × 10^{15} cm^{-3} to 3.17 × 10^{15} cm^{-3} with increasing T_s from 300 to 573 K, beyond which it increased to 3.40 × 10^{15} cm^{-3} at 623 K. Similarly, μ_h was found to increase from 0.29 cm^2 V^{-1} s^{-1} to 3.32 cm^2 V^{-1} s^{-1} with increasing T_s from 300 to 573 K as a result of the reduction in grain boundary area because of an increase in crystallite size in these films, beyond which it decreased to 2.90 cm^2 V^{-1} s^{-1} at 623 K, which can be attributed to an overall increase in the grain boundary area due to the slight decrease in the crystallite size (increasing the grain boundary scattering). Subsequently, ρ decreased from 3.42 × 10^3 Ω cm at T_s = 303 K to 0.632 × 10^3 Ω cm at T_s = 623 K. It has been stated in numerous SnS thin film studies that the carrier mobility of films increases with increasing crystallite size.[31–33] Issei Suzuki *et al.* studied the temperature dependent carrier mobility of SnS films and found grain boundary scattering dominating the carrier transport in these films.[34] Binqiang Zhou also investigated the transport properties of SnS, in which grain boundary scattering was found to strongly influence these transport properties at or below room temperature, whereas acoustic phonons[35] were found to be the dominant scattering of holes at higher temperature (*i.e.*, 400 K).

The varying electrical properties of these films can be attributed to the chemical composition (Sn/S ratio) that in turn induces Sn vacancies in these films. Note that Sn vacancies within these films induce the p-type characteristic.[4] The formation of an

Table 1 Elemental compositions as measured by XPS and EDS, along with their corresponding Sn–S atomic ratios, and electronic properties such as the electrical resistivity (ρ), carrier concentration (p_h), and carrier mobility (μ_h) of SnS films as determined by a Hall effect measurement system

	XPS(EDS)-measured composition			Electronic properties		
	Sn (at%)	S (at%)	Sn–S ratio	ρ (Ω cm)	p_h (× 10^{15} cm^{-3})	μ_h (cm^2 V s^{-1})
T_s = 303 K	52.0(54.3)	48.0(45.7)	1.1(1.2)	3420	6.13	0.29
T_s = 573 K	54.9(55.6)	45.1(44.4)	1.2(1.3)	592	3.17	3.32
T_s = 603 K	55.1(55.9)	44.9(44.1)	1.2(1.3)	632	3.4	2.9

increased Sn-rich (or S-deficient) film with increasing T_s can be attributed to the high volatility of sulfur. First-principles calculations on point defects in SnS[4] predicted the spontaneous formation of Sn^{2+} vacancies in Sn-rich SnS due to their lower formation energies. In the calculations, these Sn vacancies form at the shallow acceptor levels, thereby giving rise to p-type conductivity in these films. The observed decrease in hole concentration in the SnS film with increasing T_s could be associated with a reduction in Sn vacancies because of the increased Sn atomic ratio (or Sn-to-S-atomic ratio). Formation of Sn vacancies in Sn-rich SnS implied the presence of these excess Sn atoms (apart from those in Sn lattice sites in SnS) either in interstitials (*i.e.*, Sn interstitials (Sn_i)) or in S lattice positions (*i.e.*, Sn antisites; Sn_S). Moreover, the overall S-deficient SnS films and the comparatively lower formation energies of sulfur vacancies (V_s) and Sn_S over Sn_i suggest a higher possibility of the formation of V_s and Sn_S in these SnS films. Nevertheless, the presence of Sn_i in these SnS films cannot be ignored entirely. As shown in the first-principles calculations by Brad. D. Malone *et al.*,[4] the electronic defect states caused by the presence of V_s, Sn_S and/or Sn_i in Sn-rich SnS are formed at the donor levels.

Burton *et al.* determined the defect energy and defect concentrations of Sn and S vacancies in tin monosulphide. According to their calculations, the concentration of S vacancies is 10^7 times lower than that of Sn vacancies with the defect energy of Sn and S vacancies being 0.78 and 2.17 eV. This low defect energy of Sn vacancies leads to the formation of higher concentration of Sn vacancies at the shallow acceptor level, resulting in p-type conductivity in SnS, irrespective of Sn rich or S rich conditions.[36] Vidal *et al.* projected Sn rich conditions resulting in the accumulation of Sn into interstitials, antisites and/or grain boundaries. Additionally, they also predicted that these excess Sn atoms (with the +2 oxidation state) undergo a relaxation phenomenon and get converted to Sn donor states with an oxidation state of +4. The experimental identification of these point defects in SnS based materials was done by photoluminescence measurements in the literature.[3] Arepalli *et al.* observed red and orange emission peaks in the photoluminescence spectra of SnS particles, which they assigned to tin/sulfur vacancies, tin interstitials and/or other crystallographic defects.[37] Ghosh *et al.* also observed emission peaks at about red and near the infrared region for SnS films deposited on glass. They have also ascribed these peaks to tin vacancies, interstitials and stacking faults which are generally formed during the growth process.[38] The presence of dislocations also affects the electronic properties of SnS. The dislocation density (δ) can be evaluated using the Williamson and Smallman formula, $\delta = 1/D^2$. The dislocation densities of the SnS films deposited at T_s of 303 K, 573 K, and 623 K in this study corresponded to 2.1×10^{-3}, 0.9×10^{-3} and 1.0×10^{-3} nm^{-2}, respectively. These values are comparatively smaller, indicating that deposited layers contained densely packed grains with minimum line defects. P. A. Nwofe *et al.* also calculated a δ value of 2.2×10^{-2} nm^{-2} for SnS thin films deposited by a thermal evaporation method at 623 K on the SLG substrate.[39]

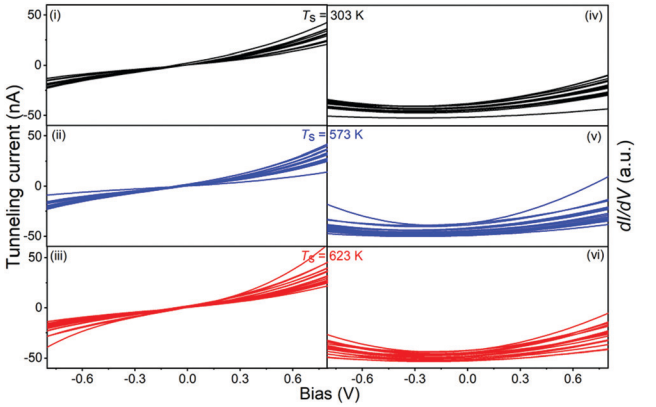

Fig. 4 (i–iii) Local STS *I*–*V* curves and (iv–vi) d*I*/d*V* curves of SnS thin films deposited on soda lime glass substrates at T_s of 303 K, 573 K, and 623 K, respectively.

SnS thin films were also characterized in the scanning tunnelling spectroscopy mode by recording the tunnelling current with respect to the sample voltage from 21 different points and their corresponding tunnelling conductance (d*I*/d*V*), which represent the local density of states of the sample (see Fig. 4(i–vi)). The tunnelling current (*I*) is related to the charge carrier density and transmission coefficient *via*

$$I \propto \int_0^{eV} \rho_{tip}(E - eV)\rho_{sample}(E)T'(E, eV, d)\mathrm{d}E, \qquad (6)$$

where $\rho_{sample}(E)$ and $\rho_{tip}(E)$ are respectively the density of states for the sample and the tip, V is the bias voltage, E is the electron energy, $T(E, eV, d)$ is the tunnelling transmission probability, and d is the sample to tip distance. Assuming the effects of ρ_{tip} and $T(E, eV, d)$ to be negligible, I can be directly proportional to only ρ_{sample}.[40]

Note that all the films showed a non-zero conductance region around the Fermi level, indicating their semi-metallic nature. To quantify, the average tunnelling current was determined by averaging the local tunnelling current values at 0.5 V. This average tunnelling current was found to increase with increasing T_s from 8 to 17 nA. This increasing local tunnelling current in these semi-metallic films with increasing T_s may be associated with the change in the (local) surface electronic structure of these enhanced Sn-rich SnS thin films due to the formation of a higher number of point defects (*i.e.*, V_{Sn}, V_S, Sn_S and/or Sn_i; see Section 3.2).

3.2. Defect thermodynamics and electronic structure

The lattice parameters and the band gap of the bulk SnS were computed to validate the reliability of the present computational approach, which is given in Table 2. The lattice parameters agreed with those of the literature reports.[33–35] In contrast, the DFT band gap was found to be underestimated. As is well known, this can be attributed to the functional derivative discontinuity of the PBE functional[42] and the delocalization error.[41]

Bulk SnS was found to be an indirect band gap semiconductor with a band gap of 0.9235 eV (Fig. 5(a)); the valence band

Table 2 Lattice parameters (in Å) and computed band gaps (in eV) of the bulk SnS

	Lattice parameters			
	a	*b*	*c*	Band gap
Current computational work	11.41	4.026	4.427	0.9235
Other computational work[43]	11.202	4.023	4.459	0.92
Experimental value[44,45]	11.1923	3.9838	4.3291	1.25

was found to be mainly composed of the S 3p orbital along with a minor contribution from Sn 5s; the conduction band was found to primarily consist of Sn 5p and a minor contribution of S 3p orbitals (see Fig. 5(b)). The electronic structure and the PDOS of the bulk SnS slab with the (111) surface orientation showed similar features and orbital compositions to those of the bulk SnS, but with a reduced band gap of 0.75 eV (see Fig. 6(a and b)).

For surface calculation, all the atoms of the top two slabs of surface supercells, which were obtained by terminating the (111) surface of the bulk SnS, were relaxed by keeping their lattice parameters fixed. These optimized surface structures (after relaxation) and the position of defects are presented in Fig. 7(j). The geometry optimization of these atoms caused surface reconstruction for all these configurations; the atomic displacements are reported in Tables S2–S11 in the ESI.†

The optimized surface structure of the SnS (111) surface (see Fig. 7(a)) showed an outward displacement of the surface atoms (towards the vacuum), except the Sn4 atom, which was found to have penetrated inside the slab to minimize the energy of the system.[46] Moreover, the SnS (111) surface was found to have almost the same orbital contributions to its valence band (VB) and conduction band (CB) as that of the bulk SnS (see Fig. 8(a)). The band structure revealed the surface to be a direct band gap semiconductor with a band gap of 0.2344 eV (Fig. 9(a)), which is contrary to that obtained for its bulk (Subsection 2.1). The surface associated band line appeared just below and above the bandgap ends in the band structure. This is consistent with the reported study for the low index surface in SnS.[47] More precisely, it was found that the lowest VB (*i.e.*, in the energy range of −2.5 to −2 eV) mainly consisted of S 3p and Sn 5p occupied states, whereas the highest VB (*i.e.*, in the energy range of −2 to 0 eV) consisted of S 3p, Sn 5s, and Sn 5p occupied states. The CB (*i.e.*, in the energy range of 0 to 2.5 eV) of the SnS (111) surface were mainly composed of Sn 5p and S 3p unoccupied states. The SnS (111) surface was found to have almost the same orbital contributions to both the valence band maximum (VBM) and conduction band minimum (CBM) as that of its bulk. In contrast, the DOS peaks of the SnS (111) surface were found to show sharp peaks (unlike bulk), which could be attributed to localized electronic states indicating a mixed ionic–covalent type of bonding.[48]

Table 3 lists the formation energies of all the above-mentioned native defect states at their preferred sites (see Section 2) evaluated from eqn (1) under both Sn-rich and S-rich conditions. Although all these native defects were found to be favorable, sulfur vacancies (V_S) and sulfur antisites (S_{Sn}) were found to be the most favorable under Sn-rich and S-rich conditions respectively.

In contrast to the PDOS of the pristine SnS (111) surface, DOS peaks corresponding to S 3p, Sn 5s, and Sn 5p unoccupied states above the Fermi level were observed in PDOS of the defective SnS (111) surface with V_{Sn} (see Fig. 8(b)). The band structure showed its band gap to be 0.48 eV and the above-mentioned unoccupied states were found to cross the Fermi level in the *k*-point path of *H*–*Y*–*Γ* as shown in Fig. 9(b). Moreover, the band line that was found to cross the Fermi line was attributed to the surface dangling bond because of Sn vacancies (Fig. 7(b)).[49] Additionally, the states formed above the Fermi level (*i.e.*, acceptor states) could cause p-type conductivity in the material system.

In the case of the SnS (111) surface with V_S, the atoms (*i.e.*, Sn2, Sn3, and Sn4 atoms) adjacent to the vacancy defect were found to move away due to the repulsion of these cations (Fig. 7(c)).[49] The contribution of DOS obtained from this defective surface with V_s was found to be similar to that of the pristine surface, but with a missing sharp Sn 5p peak at the CBE and a direct band gap of 0.213 eV (see Fig. 8(c) and 9(c)). An additional band line was obtained at the VBE of the band structure in Fig. 9(c) because of S vacancies. This band line can

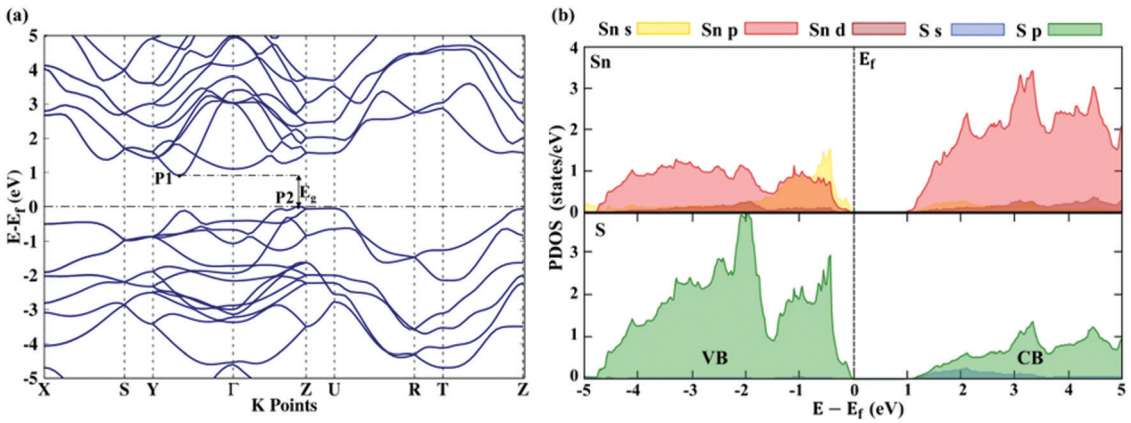

Fig. 5 (a) Electronic band structures (P1 and P2 are the conduction band minima and valence band maxima, respectively; E_g is the band gap) and (b) partial density of states (PDOS) of the bulk SnS (the dotted lines here represent the Fermi level (E_f), and these have been set to zero in the energy scale).

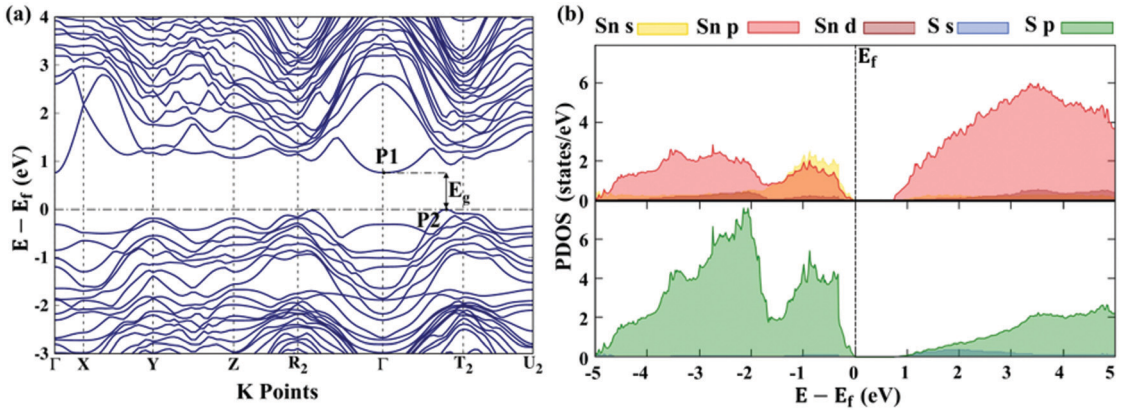

Fig. 6 (a) Electronic band structures (P1 and P2 are the conduction band minima and valence band maxima, respectively; E_g is the band gap) and (b) PDOS of the bulk (111) SnS (the dotted lines represent the Fermi levels (E_f) that are set to zero in the energy scale).

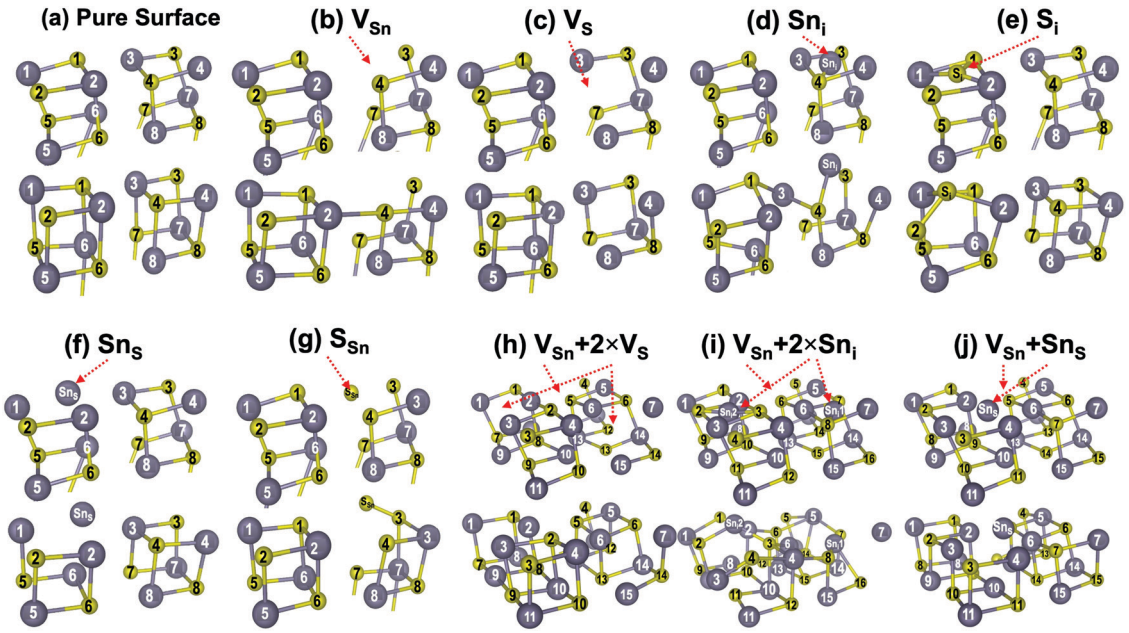

Fig. 7 SnS (111) surfaces with different structure configurations ((a) pure surface, (b) V_{Sn}, (c) V_S, (d) Sn_i, (e) S_i, (f) Sn_S and (g) S_{Sn}, (h) V_{Sn} +2 × V_S, (i) V_{Sn} +2 × Sn_i, and (j) V_{Sn} + Sn_S). The top and bottom slab structures of each configuration show the structures before and after relaxation, respectively. The grey and yellow balls shown are Sn and S atoms, respectively. The arrows denote the location of the surface defects.

act as an electron trap. A similar observation has also been reported in the literature, which carried out first principles DFT calculations on bulk SnS.[3,4] Moreover, the defective surface with V_s was found to have the lowest formation energy under Sn-rich conditions (see Table 3), which is comparable to the study conducted by Vidal *et al.* on the bulk SnS system.[3]

In the case of interstitials, the adatom (*i.e.*, Sn_i) in the reconstructed SnS surface with Sn_i showed a large displacement of 1.39 Å towards the vacuum, which could be attributed to the repulsion of Sn_i from the neighboring Sn atoms (see Fig. 7(d)). Moreover, the change in the surface structure due to the reconstruction resulted in an increase in the band gap to 0.381 eV as compared to that of the pure SnS (111) surface. Additionally, both the highest occupied and lowest unoccupied DOS states were found to be similar to that of the pure SnS surface, with the exception of the Sn 5p states, which was observed in the energy range of −0.1 to −0.3 eV. Furthermore, the band structure showed a peak near to the Fermi line at a high symmetry point X because of the Sn 5p state. Similarly, the adatom (*i.e.*, S_i) in the SnS (111) surface structure with S_i as shown in Fig. 7(e) was found to displace upward by 0.947 Å and was attributed to the strong repulsion from the neighboring S atoms. Moreover, the DOS structure was found to be similar to that of the pure SnS (111) surface, except for the sharp Sn 5p peak at the CBE. Furthermore, the defective surface with S_i showed a direct band gap of 0.201 eV at the C point (see Fig. 9(e)).

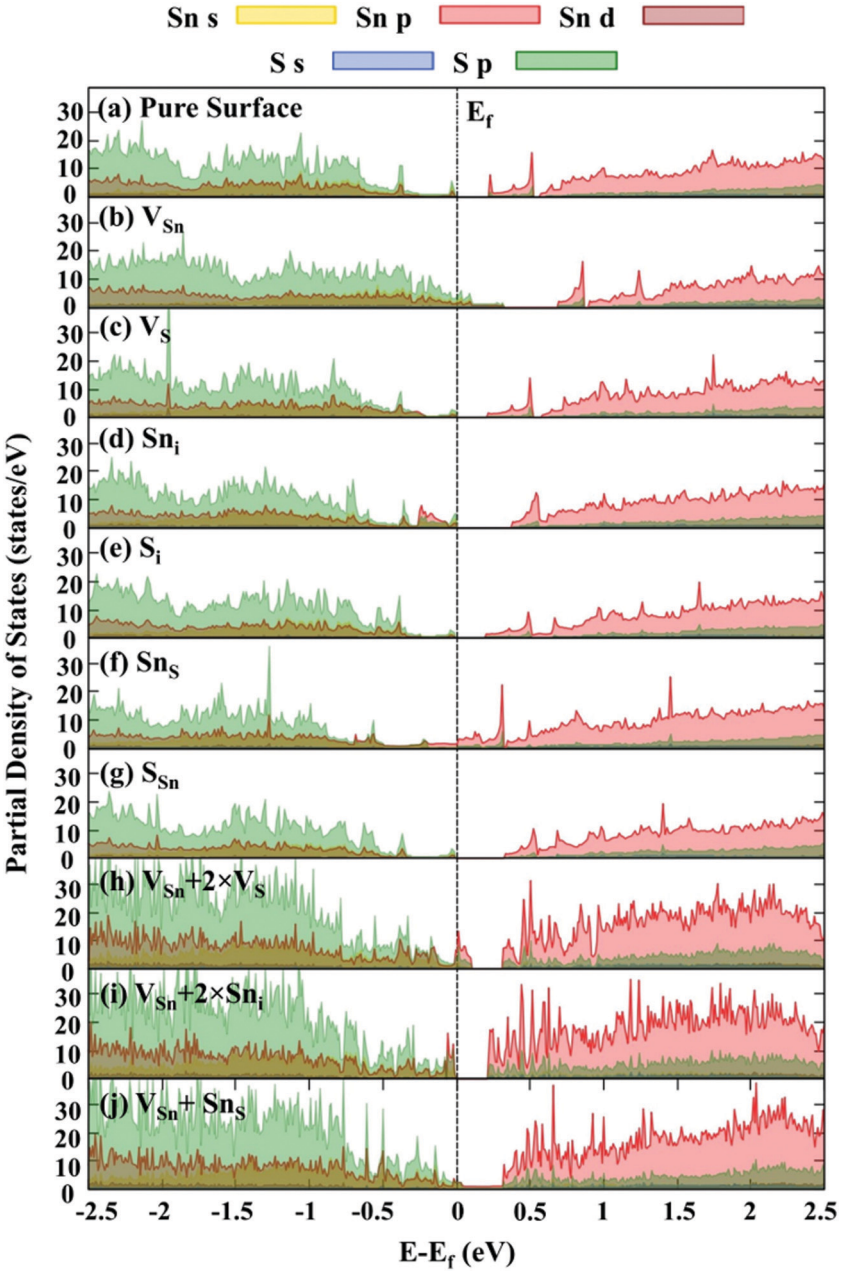

Fig. 8 PDOS on different SnS (111) surface structure configurations: (a) pure surface, (b) V_{Sn}, (c) V_S, (d) Sn_i, (e) S_i, (f) Sn_S and (g) S_{Sn}, (h) V_{Sn} + 2 V_S, (i) V_{Sn} + 2 Sn_i, (j) V_{Sn} + Sn_S (the dotted lines represent the Fermi levels that are set to zero in the energy scale).

In the case of the Sn_S defect, the band gap disappeared because of the overlapping of VB and CB (see Fig. 8(f) and 9(f)). As a result, this surface configuration would exhibit a metallic character. Its DOS below and above the Fermi level in the energy range of −0.2 to 3 eV was found to be composed of mainly Sn 5p along with minor contribution from S 3p states. Note that its lowest VB (*i.e.*, in the energy range of −3 to −0.2 eV) was found to be similar to that of the pristine SnS (111) surface. As evident from Fig. 8 (g) and 9(g), the orbital contribution of the SnS (111) surface with S_{Sn} at the VBE and CBE as well as its band structure was found to be similar to that of the pristine surface. Moreover, a direct band gap of 0.33 eV is found at the C point (see Fig. 9(g)).

As shown in Subsection 3.1, the experimentally fabricated SnS thin films were found to be Sn-rich and p-type (because of the presence of Sn vacancies as V_{Sn} has been found to form acceptor states). Additionally, as observed using the DFT calculation in this study, defects like V_S, Sn_i, and Sn_S could easily form owing to their low formation energy under Sn-rich conditions (see Table 3). These findings motivated us to further calculate multiple surface native defects for conditions favoring Sn-rich along with Sn vacancies: (i) V_{Sn} + 2 × V_S, (ii) V_{Sn} + 2 × Sn_i and (iii) V_{Sn} + Sn_S.

(i) In the case of V_{Sn} + 2 × V_S defects, the unoccupied states of Sn 5p (major) and S 3p (minor) were found to form above the

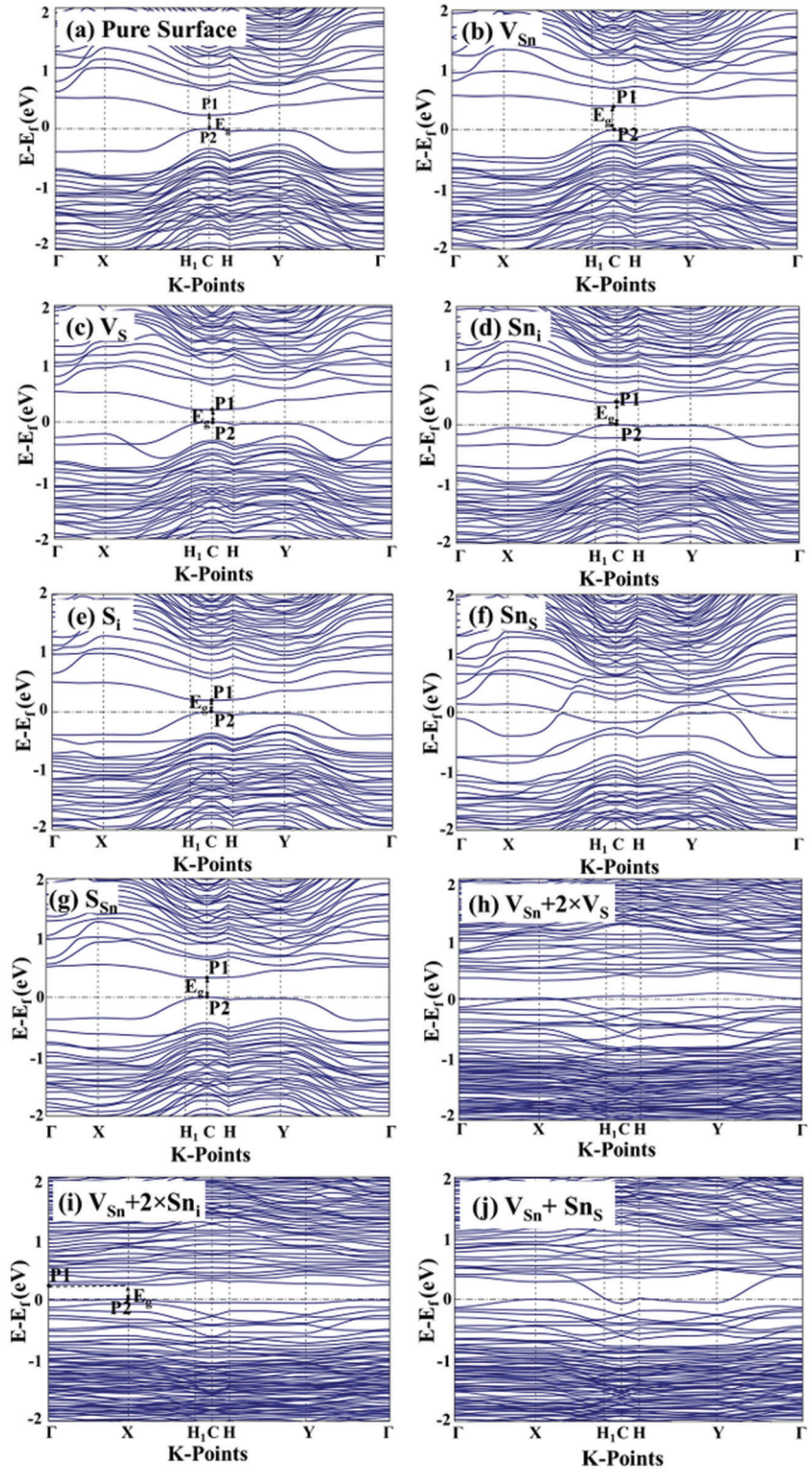

Fig. 9 Electronic band structures of SnS (111) surfaces with different structure configurations ((a) pure surface, (b) V_{Sn}, (c) V_S, (d) Sn_i, (e) S_i, (f) Sn_S and (g) S_{Sn}, (h) V_{Sn} +2 × V_S, (i) V_{Sn} +2 × Sn_i, and (j) V_{Sn} + Sn_S) (P1 and P2 are the conduction band minima and valence band maxima, respectively; E_g is the band gap).

Fermi level (see Fig. 8(h)). These unoccupied states were found to have crossed the Fermi level in the k-point path of X–C–Γ (see Fig. 9(h)), thereby reducing the band gap (0.21 eV) compared to V_{Sn} (0.48 eV).

(ii) The V_{Sn} + 2 × Sn_i defect configuration had an indirect band gap of 0.2216 eV (see Fig. 9(i)), whereas the single native Sn_i defect had a direct band gap of 0.381 eV, though their relative contributions were found to be similar (see Fig. 8(i)).

Table 3 Defect formation energy

Defect	Formation energy (eV)	
	Sn-rich	S-rich
V_{Sn}	1.4123	0.5054
V_S	0.5456	1.4525
Sn_i	0.8847	1.7916
S_i	1.4273	0.5204
Sn_S	0.9520	2.7659
S_{Sn}	2.0551	0.2412
$V_{Sn} + 2 \times V_S$	7.9627	8.8696
$V_{Sn} + 2 \times Sn_i$	12.9152	13.8221
$V_{Sn} + Sn_S$	7.5144	8.4214

(iii) In the case of $V_{Sn} + Sn_S$ defects, the VB and CB were found to be overlapping (see Fig. 8(j) and 9(j)), indicating their metallic characters. The orbital contributions to the VB in the surface with $V_{Sn} + Sn_S$ were found to be similar to those in the pristine surface; the DOS above the Fermi level (*i.e.*, CB) was found to be similar to that of the defective surface with Sn_S. Additionally, the smaller Sn 5p DOS peaks in the energy range of 0 to 0.2 eV were found for the SnS surface with $V_{Sn} + Sn_S$ (unlike with the PDOS of the Sn_S defect configuration).

3.3. Correlating the experimental observations with the computational data

In this study, thin SnS films were fabricated on cleaned soda lime glass substrates by varying the substrate temperature in the range of 303 to 623 K for 60 minute using RF magnetron sputtering. Note here that RF magnetron sputtering is a non-equilibrium thin film deposition process, in which there is a high chance for the formation of a large number of native defects.[50] As evidenced experimentally from the p-type conductivity that was induced in all these thin films in the bulk, along with their Sn-rich SnS phase (both in their bulk and at their surfaces; see Table 1), these films came across to contain a range of native defects, in the form of Sn vacancies, Sn interstitials, Sn antisites, and/or S vacancies (see Subsection 3.1). In addition to the above, though the bulk of these films demonstrated semiconducting behavior, their surfaces measured using STS showed semi-metallic characteristics (see Fig. 3 and 4). These experimental results could speculate the extension of these native defect states from the bulk of these semiconductors to their surfaces, thereby providing continuous pathways during the measurement of tunnelling current using STS, thus resulting in the semi-metallic behavior (see Fig. 4). Moreover, these experimental observations and/or discrepancies between the bulk and the surfaces of these semiconductor thin films could be supported using the findings of theoretical computations performed in this study. As shown in the computational results in Subsection 3.2 using first principles DFT, these native defects of vacancies, interstitials, and antisites have low formation energies and thus are favorable to form under these experimental conditions (see Table 3). The presence of these defects in the SnS bulk gave its p-type characteristic (along with varying hole concentration with respect to the deposition conditions); their presence on the surfaces led to the formation of the defect states, which altered their surface electronic structures and their surface band gaps. Moreover, the experimental observations and the computational predictions for the bulk and the surfaces of these SnS films were found to be in good agreement with each other.

4. Conclusions

We have, for the first time, investigated the anomalies in the bulk and the surface electrical properties of SnS taking into account various types of surface defects, based on a combinatorial approach of experiment and theory. Experimentally, single phase polycrystalline SnS films were fabricated on the SLG substrates by varying the substrate temperature from 303 to 623 K for 60 min and using SnS ceramic targets in RF magnetron sputtering. All the films were found to have grown in the SnS orthorhombic crystal structure with the strong (111) orientation of crystallites. These films were found to be Sn rich and of p-type, suggesting the presence of several native defects. Although the bulk SnS showed an optical band gap in the range of 1.61 to 1.31 eV, depicting semiconducting behavior, STS measurements demonstrated these surfaces as semi-metallic. Our first-principles DFT calculations showed a significant variation in the surface electronic structure of (111) SnS as compared to its bulk, leading to a decrease in the surface band gap (0.2344 eV as compared to 0.9235 eV for the bulk). The presence of various native surface defects – vacancies, interstitials, and antisites of both tin and sulfur – further modified the electronic structure and the band gap, by creating impurity states, which caused metallic behavior in some cases. Physico-chemical insights developed through this work can help in understanding the transport properties in a heterostructure and then play a significant role in designing high performance devices.

Author contributions

Rohit Dahule: conceptualization, methodology, formal analysis, investigation, writing – original draft, visualization. Chetan C. Singh: conceptualization, methodology, formal analysis, investigation, writing – original draft. Kenta Hongo: resources, writing – review and editing, funding acquisition. Ryo Maezono: resources, writing – review and editing, funding acquisition. Emila Panda: conceptualization, methodology, validation, resources, writing – review and editing, supervision, project administration, funding acquisition.

Conflicts of interest

There are no conflicts to declare.

Acknowledgements

The computations in this work were performed using the facilities of RCACI (Research Center for Advanced Computing Infrastructure) at JAIST. K. H. is grateful for financial support from the HPCI System Research Project (Project ID: hp190169),

MEXT-KAKENHI (JP16H06439, JP17K17762, JP19K05029, and JP19H05169), and the Air Force Office of Scientific Research (Award Numbers: FA2386-20-1-4036). R. M. is grateful for financial support from MEXT-KAKENHI (JP19H04692 and JP16KK0097), FLAGSHIP2020 (project no. hp190169 and hp190167 at K-computer), the Air Force Office of Scientific Research (AFOSR-AOARD/FA2386-17-1-4049 and FA2386-19-1-4015), and the JSPS Bilateral Joint Projects (with India DST). E.P. gratefully acknowledges financial support from the Science and Engineering Research Board, Department of Science and Technology, Government of India (Project no: EMR/2016/001182). R. D. and C. C. S. would like to gratefully acknowledge the financial support from the Japan Student Services Organization (JASSO) and the Ministry of Human Resource and Development (MHRD), Government of India, respectively.

References

1 A. de Kergommeaux, M. Lopez-Haro, S. Pouget, J.-M. Zuo, C. Lebrun, F. Chandezon, D. Aldakov and P. Reiss, Synthesis, Internal Structure, and Formation Mechanism of Monodisperse Tin Sulfide Nanoplatelets, *J. Am. Chem. Soc.*, 2015, **137**(31), 9943–9952, DOI: 10.1021/jacs.5b05576.

2 P. Sinsermsuksakul, L. Sun, S. W. Lee, H. H. Park, S. B. Kim, C. Yang and R. G. Gordon, Overcoming Efficiency Limitations of SnS-Based Solar Cells, *Adv. Energy Mater.*, 2014, **4**(15), 1400496, DOI: 10.1002/aenm.201400496.

3 J. Vidal, S. Lany, M. d'Avezac, A. Zunger, A. Zakutayev, J. Francis and J. Tate, Band-Structure, Optical Properties, and Defect Physics of the Photovoltaic Semiconductor SnS, *Appl. Phys. Lett.*, 2012, **100**(3), 32104, DOI: 10.1063/1.3675880.

4 B. D. Malone, A. Gali and E. Kaxiras, First Principles Study of Point Defects in SnS, *Phys. Chem. Chem. Phys.*, 2014, **16**(47), 26176–26183, DOI: 10.1039/C4CP03010A.

5 H. Xin, S. M. Vorpahl, A. D. Collord, I. L. Braly, A. R. Uhl, B. W. Krueger, D. S. Ginger and H. W. Hillhouse, Lithium-Doping Inverts the Nanoscale Electric Field at the Grain Boundaries in Cu2ZnSn(S{,}Se)4 and Increases Photovoltaic Efficiency, *Phys. Chem. Chem. Phys.*, 2015, **17**(37), 23859–23866, DOI: 10.1039/C5CP04707B.

6 M. Salvador, S. M. Vorpahl, H. Xin, W. Williamson, G. Shao, D. U. Karatay, H. W. Hillhouse and D. S. Ginger, Nanoscale Surface Potential Variation Correlates with Local S/Se Ratio in Solution-Processed CZTSSe Solar Cells, *Nano Lett.*, 2014, **14**(12), 6926–6930, DOI: 10.1021/nl503068h.

7 D. Azulay, O. Millo, I. Balberg, H.-W. Schock, I. Visoly-Fisher and D. Cahen, Current Routes in Polycrystalline CuInSe2 and Cu(In,Ga)Se2 Films, *Sol. Energy Mater. Sol. Cells*, 2007, **91**(1), 85–90, DOI: 10.1016/j.solmat.2006.08.006.

8 J. E. Inglesfield, Surface Electronic Structure, *Rep. Prog. Phys.*, 1982, **45**(3), 223–284, DOI: 10.1088/0034-4885/45/3/001.

9 Y. Kumagai, L. A. Burton, A. Walsh and F. Oba, Electronic Structure and Defect Physics of Tin Sulfides: SnS, Sn2 S3, and Sn S2, *Phys. Rev. Appl.*, 2016, **6**(1), 1–14, DOI: 10.1103/PhysRevApplied.6.014009.

10 W. Kohn and L. J. Sham, Self-Consistent Equations Including Exchange and Correlation Effects, *Phys. Rev.*, 1965, **140**(4A), A1133–A1138, DOI: 10.1103/PhysRev.140.A1133.

11 P. Hohenberg and W. Kohn, Inhomogeneous Electron Gas, *Phys. Rev.*, 1964, **136**(3B), B864–B871, DOI: 10.1103/PhysRev.136.B864.

12 K. Momma and F. Izumi, {\it VESTA3} for Three-Dimensional Visualization of Crystal, Volumetric and Morphology Data, *J. Appl. Crystallogr.*, 2011, **44**(6), 1272–1276, DOI: 10.1107/S0021889811038970.

13 G. Kresse and J. Hafner, Ab Initio Molecular Dynamics for Liquid Metals, *Phys. Rev. B: Condens. Matter Mater. Phys.*, 1993, **47**(1), 558–561, DOI: 10.1103/PhysRevB.47.558.

14 G. Kresse and J. Furthmüller, Efficiency of Ab-Initio Total Energy Calculations for Metals and Semiconductors Using a Plane-Wave Basis Set, *Comput. Mater. Sci.*, 1996, **6**(1), 15–50, DOI: 10.1016/0927-0256(96)00008-0.

15 J. P. Perdew, K. Burke and M. Ernzerhof, Generalized Gradient Approximation Made Simple, *Phys. Rev. Lett.*, 1996, **77**(18), 3865–3868, DOI: 10.1103/PhysRevLett.77.3865.

16 P. E. Blöchl, Projector Augmented-Wave Method, *Phys. Rev. B: Condens. Matter Mater. Phys.*, 1994, **50**(24), 17953–17979, DOI: 10.1103/PhysRevB.50.17953.

17 J. D. Pack and H. J. Monkhorst, ''special Points for Brillouin-Zone Integrations''-a Reply, *Phys. Rev. B: Solid State*, 1977, **16**(4), 1748–1749, DOI: 10.1103/PhysRevB.16.1748.

18 L. Bengtsson, Dipole Correction for Surface Supercell Calculations, *Phys. Rev. B: Condens. Matter Mater. Phys.*, 1999, **59**(19), 12301–12304, DOI: 10.1103/PhysRevB.59.12301.

19 C. Freysoldt, B. Grabowski, T. Hickel, J. Neugebauer, G. Kresse, A. Janotti and C. G. Van De Walle, First-Principles Calculations for Point Defects in Solids, *Rev. Mod. Phys.*, 2014, **86**(1), 253–305, DOI: 10.1103/RevModPhys.86.253.

20 S. Lin, C. Yeh, B. Puchala, Y.-L. Lee and D. Morgan, Ab Initio Energetics of Charge Compensating Point Defects: A Case Study on MgO, *Comput. Mater. Sci.*, 2013, **73**, 41–55, DOI: 10.1016/j.commatsci.2013.02.005.

21 B. H. Baby and D. B. Mohan, The Formation of α-Phase SnS Nanostructure from a Hybrid, Multi-Layered S/Sn/S/Sn/S Thin Films: Phase Stability, Surface Morphology and Optical Studies, *Appl. Surf. Sci.*, 2017, **423**, 1111–1123, DOI: 10.1016/j.apsusc.2017.06.291.

22 C. C. Singh, T. A. Patel and E. Panda, Relation between Surface and Bulk Electronic Properties of Al Doped ZnO Films Deposited at Varying Substrate Temperature by Radio Frequency Magnetron Sputtering, *J. Appl. Phys.*, 2015, **117**(24), 245312, DOI: 10.1063/1.4923224.

23 S. Singh, R. S. Srinivasa and S. S. Major, Effect of Substrate Temperature on the Structure and Optical Properties of ZnO Thin Films Deposited by Reactive Rf Magnetron Sputtering, *Thin Solid Films*, 2007, **515**(24), 8718–8722, DOI: 10.1016/j.tsf.2007.03.168.

24 L. Zhao, Y. Di, C. Yan, F. Liu, Z. Cheng, L. Jiang, X. Hao, Y. Lai and J. Li, In Situ Growth of SnS Absorbing Layer by Reactive Sputtering for Thin Film Solar Cells, *RSC Adv.*, 2016, **6**(5), 4108–4115, DOI: 10.1039/C5RA24144H.

25 Y. Sun, Z. Sun, S. Gao, H. Cheng, Q. Liu, F. Lei, S. Wei and Y. Xie, All-Surface-Atomic-Metal Chalcogenide Sheets for High-Efficiency Visible-Light Photoelectrochemical Water Splitting, *Adv. Energy Mater.*, 2014, **4**(1), 1300611, DOI: 10.1002/aenm.201300611.

26 J. He, L. Sun, Y. Chen, J. Jiang, P. Yang and J. Chu, Cu2ZnSnS4 Thin Film Solar Cell Utilizing Rapid Thermal Process of Precursors Sputtered from a Quaternary Target: A Promising Application in Industrial Processes, *RSC Adv.*, 2014, **4**(81), 43080–43086, DOI: 10.1039/C4RA07748B.

27 J. R. Brent, D. J. Lewis, T. Lorenz, E. A. Lewis, N. Savjani, S. J. Haigh, G. Seifert, B. Derby and P. O'Brien, Tin(II) Sulfide (SnS) Nanosheets by Liquid-Phase Exfoliation of Herzenbergite: IV–VI Main Group Two-Dimensional Atomic Crystals, *J. Am. Chem. Soc.*, 2015, **137**(39), 12689–12696, DOI: 10.1021/jacs.5b08236.

28 T. S. Reddy and M. C. S. Kumar, Co-Evaporated SnS Thin Films for Visible Light Photodetector Applications, *RSC Adv.*, 2016, **6**(98), 95680–95692, DOI: 10.1039/C6RA20129F.

29 Y. Gupta, P. Arun, A. A. Naudi, M. V. Walz and E. A. Albanesi, Grain Size and Lattice Parameter's Influence on Band Gap of SnS Thin Nano-Crystalline Films, *Thin Solid Films*, 2016, **612**, 310–316, DOI: 10.1016/j.tsf.2016.05.056.

30 P. Jain and P. Arun, Influence of Grain Size on the Band-Gap of Annealed SnS Thin Films, *Thin Solid Films*, 2013, **548**, 241–246, DOI: 10.1016/j.tsf.2013.09.089.

31 S. S. Hegde, A. G. Kunjomana, P. Murahari, B. K. Prasad and K. Ramesh, Vacuum Annealed Tin Sulfide (SnS) Thin Films for Solar Cell Applications, *Surf. Interfaces*, 2018, **10**, 78–84, DOI: 10.1016/j.surfin.2017.12.003.

32 V. K. Arepalli, Y. Shin and J. Kim, Influence of Working Pressure on the Structural, Optical, and Electrical Properties of RF-Sputtered SnS Thin Films, *Superlattices Microstruct.*, 2018, **122**, 253–261, DOI: 10.1016/j.spmi.2018.08.001.

33 Y. Kawano, J. Chantana and T. Minemoto, Impact of Growth Temperature on the Properties of SnS Film Prepared by Thermal Evaporation and Its Photovoltaic Performance, *Curr. Appl. Phys.*, 2015, **15**(8), 897–901, DOI: 10.1016/j.cap.2015.03.026.

34 I. Suzuki, S. Kawanishi, S. R. Bauers, A. Zakutayev, Z. Lin, S. Tsukuda, H. Shibata, M. Kim, H. Yanagi and T. Omata, n-Type Electrical Conduction in SnS Thin Films, *Phys. Rev. Mater.*, 2021, **5**(12), 125405, DOI: 10.1103/PhysRevMaterials.5.125405.

35 B. Zhou, S. Li, W. Li, J. Li, X. Zhang, S. Lin, Z. Chen and Y. Pei, Thermoelectric Properties of SnS with Na-Doping, *ACS Appl. Mater. Interfaces*, 2017, **9**(39), 34033–34041, DOI: 10.1021/acsami.7b08770.

36 L. A. Burton, D. Colombara, R. D. Abellon, F. C. Grozema, L. M. Peter, T. J. Savenije, G. Dennler and A. Walsh, Synthesis, Characterization, and Electronic Structure of Single-Crystal SnS, Sn2S3, and SnS2, *Chem. Mater.*, 2013, **25**(24), 4908–4916, DOI: 10.1021/cm403046m.

37 V. K. Arepalli, Y. Shin and J. Kim, Photovoltaic Behavior of the Room Temperature Grown RF-Sputtered SnS Thin Films, *Opt. Mater.*, 2019, **88**, 594–600, DOI: 10.1016/j.optmat.2018.12.016.

38 B. Ghosh, M. Das, P. Banerjee and S. Das, Fabrication of {SnS} Thin Films by the Successive Ionic Layer Adsorption and Reaction ({SILAR}) Method, *Semicond. Sci. Technol.*, 2008, **23**(12), 125013, DOI: 10.1088/0268-1242/23/12/125013.

39 P. A. Nwofe, K. T. R. Reddy, G. Sreedevi, J. K. Tan, I. Forbes and R. W. Miles, Single Phase, Large Grain, p-Conductivity-Type SnS Layers Produced Using the Thermal Evaporation Method, *Energy Procedia*, 2012, **15**, 354–360, DOI: 10.1016/j.egypro.2012.02.043.

40 C. C. Singh and E. Panda, Effect of Intrinsic Electronic Defect States on the Morphology and Optoelectronic Properties of Sn-Rich SnS Particles, *J. Appl. Phys.*, 2018, **123**(17), 174904, DOI: 10.1063/1.4994894.

41 P. Mori-Sánchez, A. J. Cohen and W. Yang, Localization and Delocalization Errors in Density Functional Theory and Implications for Band-Gap Prediction, *Phys. Rev. Lett.*, 2008, **100**(14), 146401, DOI: 10.1103/PhysRevLett.100.146401.

42 L. J. Sham and M. Schlüter, Density-Functional Theory of the Energy Gap, *Phys. Rev. Lett.*, 1983, **51**(20), 1888–1891, DOI: 10.1103/PhysRevLett.51.1888.

43 L. Pan, B. Zou and L. J. Shi, Electric Field Modulation of the Band Gap, Dielectric Constant and Polarizability in SnS Atomically Thin Layers, *Phys. Lett. Sect. A Gen. At. Solid State Phys.*, 2016, **380**(27–28), 2227–2232, DOI: 10.1016/j.physleta.2016.04.044.

44 T. Chattopadhyay, J. Pannetier and H. G. Von Schnering, Neutron Diffraction Study of the Structural Phase Transition in SnS and SnSe, *J. Phys. Chem. Solids*, 1986, **47**(9), 879–885, DOI: 10.1016/0022-3697(86)90059-4.

45 A. Sugaki, A. Kitakaze and H. Kitazawa, Synthesized Tin and Tin-Silver Sulfide Minerals. Synthetic Sulfide Minerals (XIII), *Sci. Rep.*, 1985, **16**(2), 199–211.

46 R. Dahule, A. Raghav, A. T. Hanindriyo, K. Hongo, R. Maezono and E. Panda, Surface Study of Cu_2SnS_3 Using First-Principles Density Functional Theory, *Adv. Theory Simul.*, 2021, **4**(6), 2000315, DOI: 10.1002/adts.202000315.

47 G. A. Tritsaris, B. D. Malone and E. Kaxiras, Structural Stability and Electronic Properties of Low-Index Surfaces of SnS, *J. Appl. Phys.*, 2014, **115**(17), 173702, DOI: 10.1063/1.4874775.

48 J. R. D. S. Politi, F. Viñes, J. A. Rodriguez and F. Illas, Atomic and Electronic Structure of Molybdenum Carbide Phases: Bulk and Low Miller-Index Surfaces, *Phys. Chem. Chem. Phys.*, 2013, **15**(30), 12617–12625, DOI: 10.1039/c3cp51389k.

49 S. Ciraci, I. P. Batra and W. A. Tiller, Electronic Structure of the (111) Surface of Semiconductors, *Phys. Rev. B: Solid State*, 1975, **12**(12), 5811–5823, DOI: 10.1103/PhysRevB.12.5811.

50 C. C. Singh and E. Panda, Zinc Interstitial Threshold in Al-Doped ZnO Film: Effect on Microstructure and Optoelectronic Properties, *J. Appl. Phys.*, 2018, **123**(16), 165106, DOI: 10.1063/1.5021736.